New Journal of Physics
The open-access journal for physics

Capillary instability on a hydrophilic stripe

Raymond L Speth[1] **and Eric Lauga**[2,3]

[1] Department of Mechanical Engineering, Massachusetts Institute of Technology, 77 Massachusetts Avenue, Cambridge, MA 02139, USA
[2] Department of Mechanical and Aerospace Engineering, University of California, San Diego, 9500 Gilman Dr, La Jolla, CA 92093-0411, USA
E-mail: elauga@ucsd.edu

New Journal of Physics **11** (2009) 075024 (15pp)
Received 30 January 2009
Published 31 July 2009
Online at http://www.njp.org/
doi:10.1088/1367-2630/11/7/075024

Abstract. A recent experiment showed that cylindrical segments of water filling a hydrophilic stripe on an otherwise hydrophobic surface display a capillary instability when their volume is increased beyond the critical volume at which their apparent contact angle on the surface reaches 90° (Gau *et al* 1999 *Science* **283** 46–9). Surprisingly, the fluid segments did not break up into droplets—as would be expected for a classical Rayleigh–Plateau instability—but instead displayed a long-wavelength instability where all excess fluid gathered in a single bulge along each stripe. We consider here the dynamics of the flow instability associated with this setup. We perform a linear stability analysis of the capillary flow problem in the inviscid limit. We first confirm previous work showing that all cylindrical segments are linearly unstable if (and only if) their apparent contact angle is larger than 90°. We then demonstrate that the most unstable wavenumber for the surface perturbation decreases to zero as the apparent contact angle of the fluid on the surface approaches 90°, allowing us to re-interpret the creation of bulges in the experiment as a zero-wavenumber capillary instability. A variation of the stability calculation is also considered for the case of a hydrophilic stripe located on a wedge-like geometry.

[3] Author to whom any correspondence should be addressed.

Contents

1. Introduction

Capillary instabilities are phenomena we witness in our daily lives, and their study is a field with a rich history [1]–[4]. The classical Rayleigh–Plateau instability refers to the surface-tension-induced instability of a cylindrical liquid column. For volume-preserving deformations of sufficiently long wavelengths along a fluid cylinder, the surface area of the fluid can be made to decrease. These deformations lower the surface energy of the fluid and are therefore favorable, so an infinite cylindrical fluid column is always capillary unstable. For a cylindrical fluid column of radius R, density ρ and surface tension γ, this instability is of inviscid nature, and occurs on a typical timescale $\tau_1 \sim (\rho R^3/\gamma)^{1/2}$, with the most unstable wavelength being of the order of the column radius [1, 2].

Many variations on this classical result have been considered in the past, and we refer to [1] for a review. In the present paper, we consider such instabilities when they occur for a cylindrical segment of fluid in contact with a solid. A recent experimental investigation on the stability of a cylindrical segment of liquid on a stripe of hydrophilic material on an otherwise hydrophobic surface has shown surprising long-wavelength instabilities. In that case, the fluid segment was observed not to break up in many droplets as in the classical Rayleigh–Plateau instability, but instead to form a single large bulge [5]. The purpose of this paper is to study the dynamics of such a surprising capillary instability.

A number of previous studies have approached the problem of flow stability for a cylindrical segment of fluid pinned on a solid substrate. Davis considered a flow rivulet down an incline, with its contact line pinned along a stripe [6]. Using an energy method, it was found that when the interior angle (i.e. the apparent contact angle of the rivulet on the horizontal surface) was less than 90°, the rivulet is stable, and it is unstable otherwise. A similar result was later obtained using energy minimization considerations for a cylindrical interface pinned to a slot [7]. In addition, the critical length for the instability of a finite cylinder was found to become infinite at the critical angle of 90° [7]. Similar results were later recovered using differential geometry, where volume-preserving perturbations were seen to lead to decrease in the surface area of the cylindrical filament only in the case where the apparent angle exceeded 90°, and for asymptotically large wavelengths near the threshold [8]–[12].

The experimental observations of Gau *et al* [5], which motivate the present study, are reproduced in figure 1. The fluid (water) is filling hydrophilic stripes (contact angle ≈5°) on

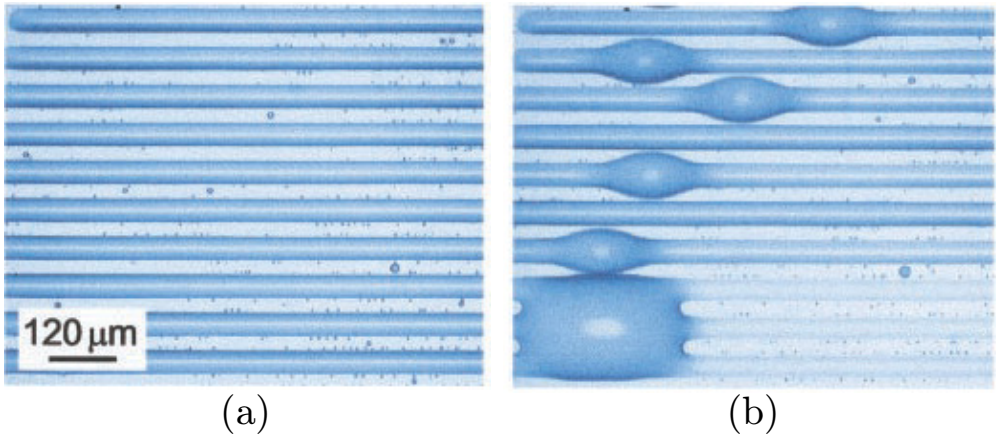

Figure 1. The growing instability of a cylindrical segment on a hydrophilic stripe. (a) For small enough volume, the cylindrical segments, located along the hydrophilic stripe and separated by hydrophobic stripes, are stable. (b) At a critical value of the fluid volume, corresponding to an apparent contact angle of the fluid of 90°, the cylindrical segment become unstable, and solitary bulges grow. Reprinted from [5], courtesy of R Lipowsky and with permission from AAAS (doi:10.1126/science.283.5398.46).

an otherwise hydrophobic substrate (contact angle ≈108°). The fluid volume is then increased. In the absence of the observed instability, a schematic representation of the growth process is represented in figure 2. As the fluid volume increases, the contact line at the edges of the cylindrical segments of water remains pinned, until the volume of fluid becomes large enough that the apparent contact angle is equal to the advancing contact angle on the hydrophobic surface. At this point, any subsequent volume change would be accompanied by a motion of the contact line into the hydrophobic substrate. The experimental result obtained by Gau *et al* is that such a process is unstable. As soon as the apparent contact angle of the fluid segment reaches the critical value of 90° (intermediate between the contact angles on both surfaces; see figure 2(c)), the surface becomes capillary unstable. This result is consistent with the previous studies discussed above [6]–[11]. Surprisingly, and in contrast with a free fluid cylinder, the observed unstable mode does not display a wavelength of the order of the cylindrical radius, but instead the wavelength appears to be much larger, and the segment evolves to a state where all the excess fluid gathers on single bulge (figure 1). Some features of these experiments were later reproduced by Darhuber *et al* in their experimental and numerical study of droplet morphologies on chemically patterned surfaces [13], and are consistent with the simplified one-dimensional stability study of [14].

The aim of the present work is to focus on the dynamics of the instability process by performing a linear stability analysis of the cylindrical segment in the experiments of Gau *et al*, and predicting the dependence of the growth rates and most unstable wavelengths of the unstable modes on the apparent contact angle of the cylindrical segment. We restrict our study to low viscosity liquids, such as water, and perform an inviscid study. Physically, inviscid capillary instabilities of a fluid column are expected to occur on a timescale $\tau_1 \sim (\rho R^3/\gamma)^{1/2}$.

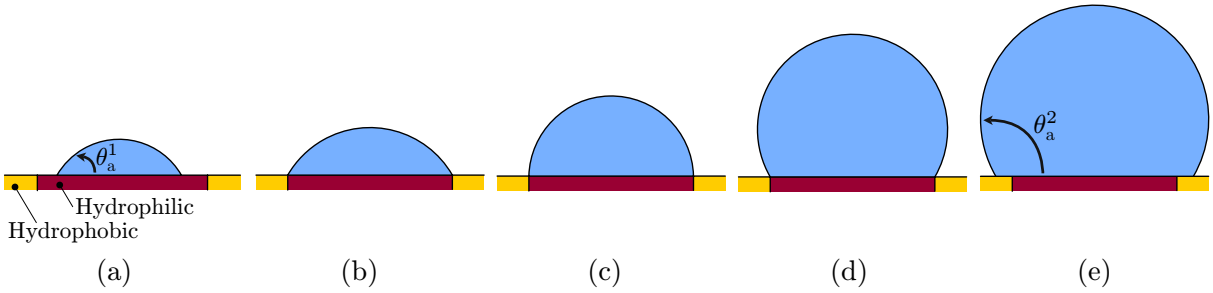

Figure 2. Schematic representation of the different stages of growth of a cylindrical segment on a hydrophilic stripe in the absence of any capillary instability. (a) For small enough volumes, the fluid grows solely on the hydrophilic region, and displays an advancing contact angle, θ_a^1. (b) At a critical fluid volume, the line separating hydrophilic and hydrophobic domains in reached. (c) As the fluid volume continues to increase, the contact line remains pinned, and the apparent angle increases. (d) The angle stops increasing when the apparent angle reaches the value, θ_a^2, of the advancing angle on the hydrophobic domain (note that $\theta_a^2 > 90^\circ > \theta_a^1$). (e) As the fluid volume continues to increase, the contact line region now moves into the hydrophobic domains, with angle θ_a^2. In this paper, we show that the cylindrical segment displays capillary instability as soon as (c) is reached (apparent angle of 90°).

For comparison, the timescale for viscous effects to propagate diffusively across the width of a fluid column is $\tau_2 \sim R^2/\nu$, where ν is the kinematic viscosity of the fluid. The inviscid approach will therefore be a reasonable modeling assumption as long as $\tau_1 \ll \tau_2$, which is equivalent to $R \gg \ell$, with $\ell = \rho\nu^2/\sigma$ is the Ohnesorge length scale of the fluid. For water, ℓ is in the tens of nanometers, which is much smaller than the typical cross-sectional size in the experiments of Gau *et al* [5] (tens of microns; see figure 1). As we show below, within these assumptions, the most unstable wavelength for the capillary instability of the cylindrical segment tends toward infinity as the contact angle approaches 90°, thereby allowing us to re-interpret the creation of bulges in the experiment as a zero-wavenumber capillary instability [5].

2. Set-up and linear stability

The geometrical set-up for our linear stability calculation is illustrated in figure 3. The basic state is a cylindrical segment of fluid of radius R, whose two-dimensional contact line is pinned along a stripe. The apparent contact angle of the fluid at the contact line is denoted θ_c. We assume θ_c to be sufficiently larger (smaller) than the receding (advancing) angle on the hydrophilic (hydrophobic) substrate so that we can safely assume that during the initial stages of the instability the contact line remains pinned along the same location. In addition, since we know from earlier work that the case where $\theta_c < 90^\circ$ is stable [6]–[11], we will focus here on determining the dynamics of the instability in the case where $\theta_c \geqslant 90^\circ$.

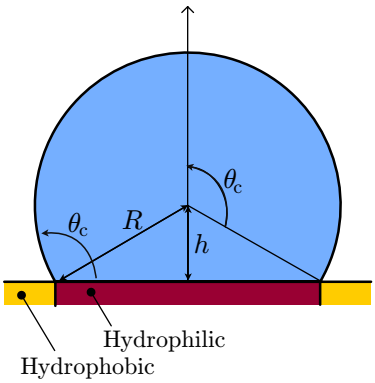

Figure 3. Set-up for the inviscid stability calculation. We consider a cylindrical segment with a pinned contact line, displaying an apparent contact angle $\theta_c \geqslant 90^\circ$. The radius of the cylindrical segment is denoted R, and the height of its center above the surface is denoted h.

2.1. Governing equations and linearization

Assuming the liquid is both incompressible and inviscid, its motion is prescribed by the Euler equation and the continuity equation,

$$\rho\left(\frac{\partial \mathbf{u}}{\partial t} + \mathbf{u}\cdot\nabla\mathbf{u}\right) = -\nabla p, \tag{1}$$

$$\nabla\cdot\mathbf{u} = 0, \tag{2}$$

where $\mathbf{u}$ and p denote the velocity and pressure fields, respectively. Since there is no flow in the basic state, the linearized equations are simply

$$\rho\frac{\partial \mathbf{u}'}{\partial t} = -\nabla p', \tag{3}$$

$$\nabla\cdot\mathbf{u}' = 0, \tag{4}$$

where primes denotes small deviations from the basic state. We employ cylindrical coordinates, and use the center of the cylindrical segment as the origin of our coordinate system; the variable z denotes therefore the coordinate along the stripe, and $\theta = 0$ denotes in the vertical direction. Let the radius of the free surface be parameterized as $\xi(t, \theta, z)$. Since the radius of the free surface is R in the basic state, then the perturbation in the position of the free surface is $\xi' = \xi - R$. The free surface moves with the local velocity of the fluid, which after linearization is written as

$$u_r'|_{r=R} = \frac{\partial \xi'}{\partial t}\cdot \tag{5}$$

Additionally, at the contact points, the position of the contact point is fixed, giving the condition

$$u_r'|_{\{r=R,\theta=\pm\theta_c\}} = 0. \tag{6}$$

The jump in pressure across the free surface is related to the curvature of the surface and the surface tension as

$$p - p_\infty = \gamma \nabla \cdot \mathbf{n}, \tag{7}$$

where the outward surface normal is given by

$$\mathbf{n} = \frac{1}{\sqrt{1 + \left(\frac{\partial \xi}{\partial z}\right)^2 + \frac{1}{r^2}\left(\frac{\partial \xi}{\partial \theta}\right)^2}} \left(\mathbf{e}_r - \frac{1}{r}\frac{\partial \xi}{\partial \theta}\mathbf{e}_\theta - \frac{\partial \xi}{\partial z}\mathbf{e}_z \right), \tag{8}$$

and the divergence of the normal is

$$\nabla \cdot \mathbf{n} = \frac{\partial n_z}{\partial z} + \frac{1}{r}\frac{\partial}{\partial r}(r n_r) + \frac{1}{r}\frac{\partial n_\theta}{\partial \theta}. \tag{9}$$

When linearized, this boundary condition becomes

$$p'|_{r=R} = -\gamma \left(\frac{\xi'}{R^2} + \frac{\partial^2 \xi'}{\partial z^2} + \frac{1}{R^2}\frac{\partial^2 \xi'}{\partial \theta^2} \right). \tag{10}$$

At the solid surface, the normal component of the velocity vanishes, and therefore

$$\mathbf{u}' \cdot \mathbf{n} = 0. \tag{11}$$

2.2. Normal modes

Taking the divergence of the linearized Euler equation, equation (3), gives the Laplace equation for the pressure,

$$\nabla^2 p' = 0. \tag{12}$$

Considering normal modes for p', $\mathbf{u}'$ and ξ' such that

$$p'(r, \theta, z, t) = \hat{p}(r, \theta) \mathrm{e}^{st + \mathrm{i}kz}, \tag{13}$$

$$\mathbf{u}'(r, \theta, z, t) = \hat{\mathbf{u}}(r, \theta) \mathrm{e}^{st + \mathrm{i}kz}, \tag{14}$$

$$\xi'(\theta, z, t) = \hat{\xi}(\theta) \mathrm{e}^{st + \mathrm{i}kz}, \tag{15}$$

equation (12) becomes

$$\frac{\partial^2 \hat{p}}{\partial r^2} + \frac{1}{r}\frac{\partial \hat{p}}{\partial r} + \frac{1}{r^2}\frac{\partial^2 \hat{p}}{\partial \theta^2} - k^2 \hat{p} = 0. \tag{16}$$

Substituting these normal modes into equation (3) relates the pressure to the velocity,

$$\rho s \hat{\mathbf{u}} = -\frac{\partial \hat{p}}{\partial r}\mathbf{e}_r - \frac{1}{r}\frac{\partial \hat{p}}{\partial \theta}\mathbf{e}_\theta - \mathrm{i}k\hat{p}\mathbf{e}_z, \tag{17}$$

allowing the boundary conditions to be expressed solely in terms of $\hat{p}$. The boundary condition for the motion of the free surface, equation (5), then becomes

$$-\frac{1}{\rho s}\frac{\partial \hat{p}}{\partial r} = s\hat{\xi}. \tag{18}$$

The stress boundary condition on the free surface, equation (10), becomes

$$\hat{p} = -\gamma \left(\frac{1}{R^2} - k^2 + \frac{1}{R^2} \frac{\partial^2}{\partial \theta^2} \right) \hat{\xi}. \tag{19}$$

Combining equations (18) and (19) to eliminate $\hat{\xi}$ leads to

$$s^2 \hat{p} = \frac{\gamma}{\rho R^2} \left(1 - k^2 R^2 + \frac{\partial^2}{\partial \theta^2} \right) \frac{\partial \hat{p}}{\partial r}. \tag{20}$$

Next, we need to express the no-penetration boundary condition at the wall in terms of $\hat{p}$. Using the relations between $\hat{p}$ and $\hat{\mathbf{u}}$ from equation (17), the no-penetration condition, equation (11), may be written as

$$\frac{\partial \hat{p}}{\partial r} n_r + \frac{1}{r} \frac{\partial \hat{p}}{\partial \theta} n_\theta = 0, \tag{21}$$

along the solid substrate. Finally, the condition that the contact points of the free surface are stationary requires

$$\frac{\partial \hat{p}}{\partial r} = 0, \tag{22}$$

at the contact points. The complete eigenvalue problem to solve for the pressure field is therefore given by equation (16), together with the boundary conditions provided by equations (20)–(22).

We may solve equation (16) by the method of separation of variables, letting $\hat{p}(r, \theta) = F(r)G(\theta)$. Applying this separation gives

$$\frac{F''}{F} + \frac{F'}{rF} - \frac{k^2}{r^2 R} = -\frac{G''}{G} = \lambda^2. \tag{23}$$

We see that equation (23) for F is the modified Bessel differential equation, whose solutions are modified Bessel functions of the first and the second kind,

$$F(r) = C_1 I_\lambda(kr) + C_2 K_\lambda(kr), \tag{24}$$

whereas the general solution to equation (23) for G is

$$G(\theta) = C_3 \sin \lambda\theta + C_4 \cos \lambda\theta. \tag{25}$$

Applying the periodicity condition, that is, $G(\theta) = G(\theta + 2\pi)$ to equation (25) gives that $\lambda_n = n$, where $n = 0, 1, 2, \ldots$. Applying the condition that $\hat{p}$ is finite at $r = 0$ to equation (24) eliminates K_λ as a solution for F. A general solution for $\hat{p}$ may then be written as

$$\hat{p}(r, \theta) = \sum_{n=0}^{\infty} I_n(kr)(A_n \sin n\theta + B_n \cos n\theta), \tag{26}$$

where A_n and B_n are series of unknown constants to be determined by the boundary conditions. Applying the boundary condition at the free surface, equation (20), with $r = R$ and $|\theta| < \theta_c$ produces

$$s^2 \sum_{n=0}^{\infty} I_n(kR)\,(A_n \sin n\theta + B_n \cos n\theta)$$
$$= \frac{\gamma}{\rho R^2} \sum_{n=0}^{\infty} k\left(1 - k^2R^2 - n^2\right) I_n'(kR)\,(A_n \sin n\theta + B_n \cos n\theta)\,. \tag{27}$$

The no-penetration condition at the lower wall, equation (21), is given by

$$\frac{\partial \hat{p}}{\partial r} + \frac{\sin\theta}{h}\frac{\partial \hat{p}}{\partial \theta} = 0, \tag{28}$$

where h is the vertical separation between the origin and the wall. Applying this condition using $r = -h/\cos\theta$ and $\theta_c < |\theta| < \pi$ produces

$$\sum_{n=0}^{\infty} kI_n'\left(-\frac{kh}{\cos\theta}\right)(A_n \sin n\theta - B_n \cos n\theta)$$
$$= -\sum_{n=0}^{\infty} \frac{n\sin\theta}{h} I_n\left(-\frac{kh}{\cos\theta}\right)(A_n \cos n\theta + B_n \sin n\theta)\,. \tag{29}$$

At the contact points, $r = R$, $|\theta| = \theta_c$, equation (22) becomes

$$\sum_{n=0}^{\infty} kI_n'(kR)\,(A_n \sin n\theta + B_n \cos n\theta) = 0. \tag{30}$$

2.3. Eigenvalue problem

Together, equations (27), (29) and (30) represent a generalized eigenvalue problem, where the eigenvalue is the square of the growth rate, s^2, and the eigenvector is composed of the series of constants A_n and B_n. Unlike many other eigenvalue problems that arise in separation of variables solutions, these equations cannot be solved in the usual manner, that is, by multiplying by one of the modes, integrating over the domain of θ and applying the orthogonality of the modes to generate analytical expressions for the constants A_n and B_n. This is because the boundary conditions in the physical problem are of mixed type.

An approximate numerical solution to the eigenvalue problem may be sought by truncating the series at $n = N$, and evaluating the boundary conditions at some number of discrete $\theta = \{\theta_1, \ldots, \theta_{2N+1}\}$ to produce a linear system of $2N+1$ equations in $2N+1$ unknowns (A_0 is irrelevant). The set of θ is picked to specifically include $\pm\theta_c$ to ensure that the boundary conditions at those points are met. Formally, the eigenvalue problem of equations (27)–(30) may be rewritten as

$$\sum_{n=0}^{\infty} A_n a_n(\theta) + B_n b_n(\theta) = s^2 \sum_{n=0}^{\infty} A_n \alpha_n(\theta) + B_n \beta_n(\theta), \tag{31}$$

where the functions a_n, b_n, α_n and β_n are given by

$$a_n = \begin{cases} \frac{\gamma}{\rho R^2} I_n'(kR)k\left(1-k^2R^2-n^2\right)\sin n\theta, & |\theta| < \theta_c, \\ kI_n'\left(-\frac{kh}{\cos\theta}\right)\sin n\theta + \frac{n\sin\theta}{h} I_n\left(-\frac{kh}{\cos\theta}\right)\cos n\theta, & |\theta| = \theta_c, \\ kI_n'(kR)\sin n\theta, & \theta_c < |\theta| < \pi, \end{cases} \tag{32}$$

$$b_n = \begin{cases} \frac{\gamma}{\rho R^2} I_n'(kR)\left(1-k^2R^2-n^2\right)\cos n\theta, & |\theta| < \theta_c, \\ kI_n'\left(-\frac{kh}{\cos\theta}\right)\cos n\theta - \frac{n\sin\theta}{h} I_n\left(-\frac{kh}{\cos\theta}\right)\sin n\theta, & |\theta| = \theta_c, \\ kI_n'(kR)\cos n\theta & \theta_c < |\theta| < \pi, \end{cases} \tag{33}$$

$$\alpha_n = \begin{cases} I_n(kR)\sin n\theta, & |\theta| < \theta_c, \\ 0, & |\theta| = \theta_c, \\ 0, & \theta_c < |\theta| < \pi, \end{cases} \tag{34}$$

and

$$\beta_n = \begin{cases} I_n(kR)\cos n\theta, & |\theta| < \theta_c, \\ 0, & |\theta| = \theta_c, \\ 0, & \theta_c < |\theta| < \pi. \end{cases} \tag{35}$$

The approximate eigenvalue problem may then be written in the matrix form as

$$\begin{bmatrix} a_1(\theta_1) & \cdots & a_N(\theta_1) & b_0(\theta_1) & \cdots & b_N(\theta_1) \\ \vdots & & \vdots & \vdots & & \vdots \\ a_1(\theta_{2N+1}) & \cdots & a_N(\theta_{2N+1}) & b_0(\theta_{2N+1}) & \cdots & b_N(\theta_{2N+1}) \end{bmatrix} \begin{bmatrix} A_1 \\ \vdots \\ A_N \\ B_0 \\ \vdots \\ B_N \end{bmatrix}$$

$$= s^2 \begin{bmatrix} \alpha_1(\theta_1) & \cdots & \alpha_N(\theta_1) & \beta_0(\theta_1) & \cdots & \beta_N(\theta_1) \\ \vdots & & \vdots & \vdots & & \vdots \\ \alpha_1(\theta_{2N+1}) & \cdots & \alpha_N(\theta_{2N+1}) & \beta_0(\theta_{2N+1}) & \cdots & \beta_N(\theta_{2N+1}) \end{bmatrix} \begin{bmatrix} A_1 \\ \vdots \\ A_N \\ B_0 \\ \vdots \\ B_N \end{bmatrix}. \tag{36}$$

The solutions to this generalized eigenvalue problem may be found using Matlab or comparable software.

3. Stability results

The results of our linear stability calculation are illustrated in figure 4, where we plot the square of the dimensionless growth rate of the most unstable mode, $s^2/(\gamma/\rho R^3)$, as a function of the dimensionless wavenumber of the perturbation, kR, for different values of the apparent contact

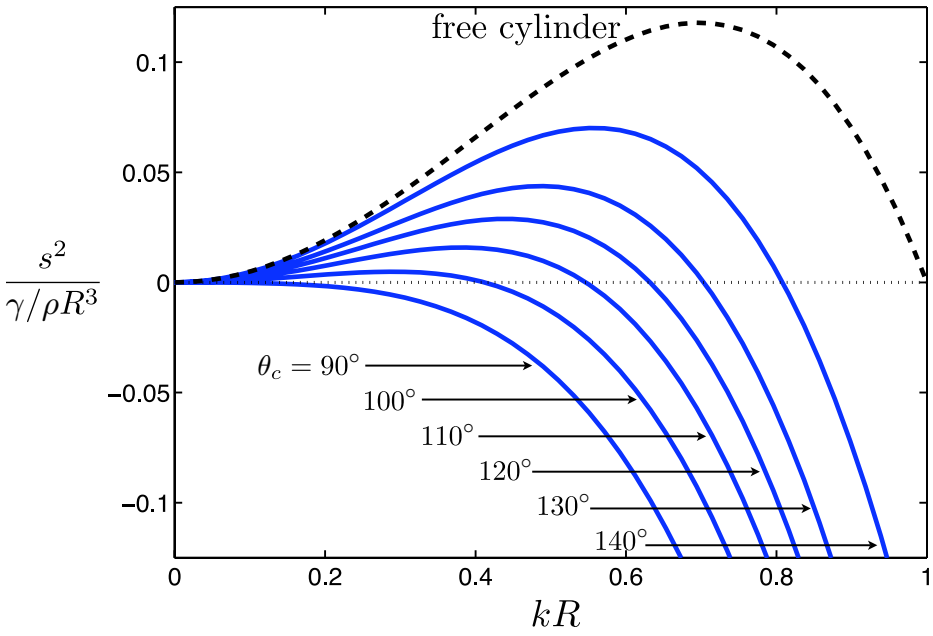

Figure 4. Capillary instability of cylindrical segment on a hydrophilic stripe: square of the dimensionless growth rate, $s^2/(\gamma/\rho R^3)$, as a function of the dimensionless wavenumber, kR, for various value of the apparent angle of the stripe, $\theta_c = 90°$, 100°, 110°, 120°, 130° and 140°. We also reproduce as a dashed line the growth rate for a free cylinder (classical Rayleigh–Plateau instability).

angle θ_c (solid lines). We also plot for comparison the result for a free cylinder, i.e.

$$s^2 = \frac{\gamma}{\rho R^3}\frac{I_0'(kR)}{I_0(kR)}\left(1-k^2R^2\right)kR, \tag{37}$$

which is the classical Rayleigh–Plateau result (dashed line) [1, 2]. An instability is possible only if there exists a value of k for which a mode of deformation satisfies $s^2 > 0$. We see in figure 4 that, in accordance with previous work, the cylindrical segments with $\theta_c > 90°$ are always linearly unstable [6], [8]–[12]. The main result of the paper, as seen in figure 4, is the explicit calculation of the range of unstable wavenumbers (together with the associated growth rates) and, in particular, the result that this range reaches zero for $\theta_c = 90°$, which coincides with the limit of the stability domain. In other words, in the experiment of [5], as soon as the apparent contact angle reaches the critical value of $\theta_c = 90°$ from below, the fluid becomes capillary unstable, but at a wavenumber that is close to zero, corresponding therefore to deformations with infinitely long wavelengths. Consequently, the experimentally observed bulges are the manifestation of a zero-wavenumber capillary instability [5]. We further plot in figure 5 the shape of the three most unstable modes for the position of the free surface $\hat{\xi}(\theta)$ for $\theta_c = 110°$ and $kR = 0.5$. Additional modes reflect higher spatial harmonics, all with negative values for s^2. In no case does the value of s^2 become positive for any mode except the first, as is the case for the Rayleigh–Plateau problem [1, 2]. Finally, we compare in figure 6 the results of our stability calculation (solid line) with that of the one-dimensional model of [14] (dashed line) for $\theta_c = 110°$. We see that the one-dimensional approximation, although qualitatively similar to the results of the full calculation, over-estimates both the growth rate and the most unstable wavenumber.

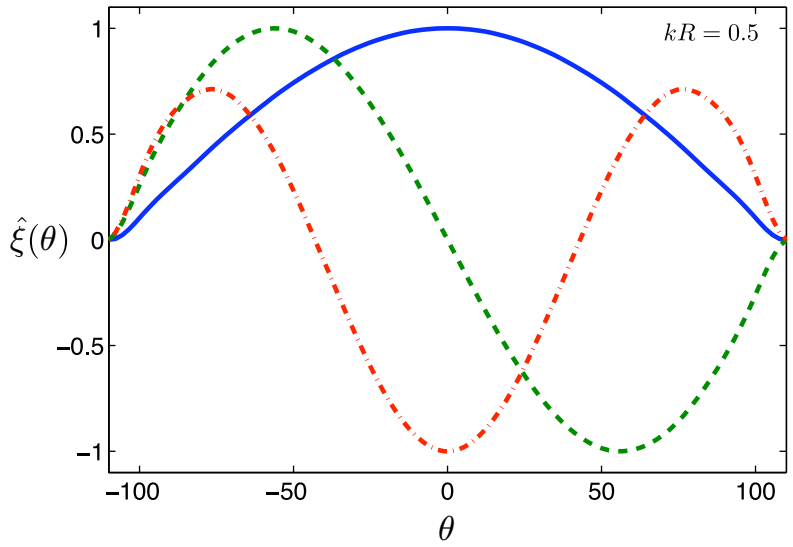

Figure 5. Normalized interfacial shapes of the modes, $\hat{\xi}(\theta)$, as a function of the angle θ about the vertical direction, for a cylindrical segment with $\theta_c = 110^\circ$, and wavenumber $kR = 0.5$. The three most unstable modes are plotted: $s^2/(\gamma/\rho R^3) = 0.008$ (solid line, blue; this is the only unstable mode), -2.539 (dashed line, green), -10.11 (dash-dotted line, red).

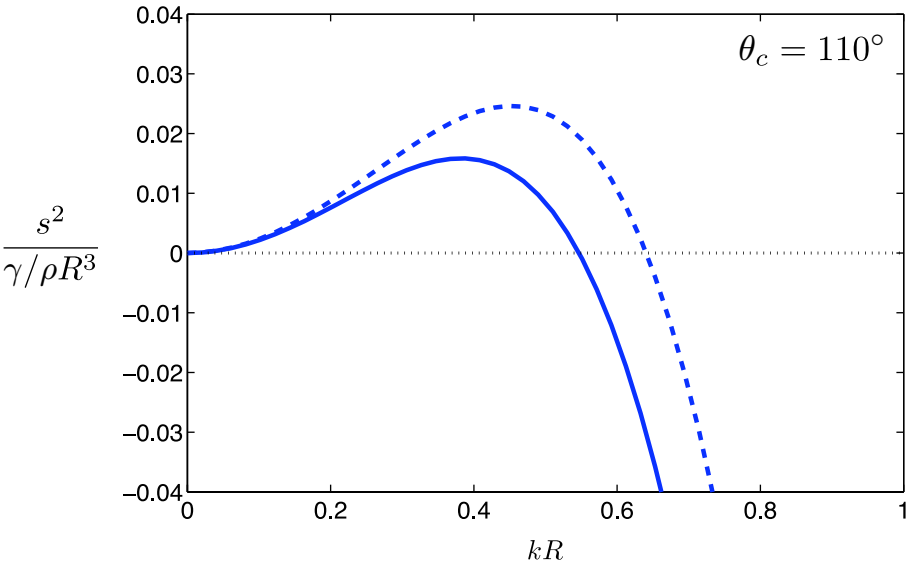

Figure 6. Comparison between the inviscid stability calculation from the present paper (solid line) and the one-dimensional inviscid model from Schiaffino *et al* [14] (dashed line) for $\theta_c = 110^\circ$. Square of the dimensionless growth rate of the most unstable mode, $s^2/(\gamma/\rho R^3)$, as a function of the dimensionless wavenumber, kR.

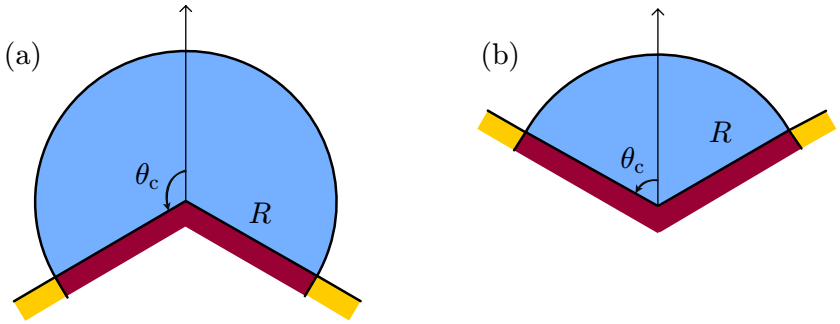

Figure 7. Fluid segment on a hydrophilic stripe on a wedge of opening angle $2\theta_c$: (a) $\theta_c > 90^\circ$ and (b) $\theta_c < 90^\circ$.

4. Cylindrical segment on a wedge

Inspired by the results above, we consider now a different geometrical set-up, as illustrated in figure 7. So far we have assumed the substrate to be horizontal. In that case, when the fluid volume is increased, both the apparent contact angle of the cylindrical segment on the surface and the cross-sectional shape of the fluid change. We now consider a set-up where the contact angle is fixed, whereas the shape is allowed to change. Specifically, we consider a cylindrical segment of fluid on a hydrophilic stripe in a wedge-like geometry. The volume of the fluid and the opening angle of the wedge, $2\theta_c$, are supposed to be such that the apparent contact angle of the fluid on the surface always remains 90°. As a result, the center of the cross section of the fluid segment is a circular wedge centered at the tip of the hydrophilic wedge (see figure 7). This geometry is reminiscent of previous work on droplets in angular geometries, in both static [15, 16] and flowing [17] conditions.

We consider therefore the capillary stability of the configuration illustrated in figure 7 with notation similar to the previous section. We now use a cylindrical coordinate system with the origin at the point of the wedge, and with $\theta = 0$ aligned with one segment of the solid wall and $\theta = 2\theta_c$ with the other. The boundary conditions in this geometry may be applied as follows. Applying the no-penetration boundary condition, equation (21), to the harmonic equation for the θ-dependence of the solution, equation (25), gives that $C_3 = 0$ and $\lambda_n = n\pi/2\theta_c$, where $n = 0, 1, 2, \ldots$. As before, requiring that $\hat{p}$ be finite at $r = 0$ requires that $C_2 = 0$. The form of the solution for $\hat{p}$ is then

$$\hat{p}(r, \theta) = \sum_{n=0}^{\infty} A_n I_{\lambda_n}(kr) \cos \frac{n\pi\theta}{2\theta_c}. \tag{38}$$

The boundary condition along the free surface, $\{r = R, 0 < \theta < 2\theta_c\}$, as given by equation (20) becomes

$$s^2 \sum_{n=0}^{\infty} A_n I_{\lambda_n}(kR) \cos \frac{n\pi\theta}{2\theta_c} = \sum_{n=0}^{\infty} \frac{\gamma}{\rho R^2} k \left(1 - k^2R^2 - \frac{n^2\pi^2}{4\theta_c^2}\right) A_n I'_{\lambda_n}(kR) \cos \frac{n\pi\theta}{2\theta_c}. \tag{39}$$

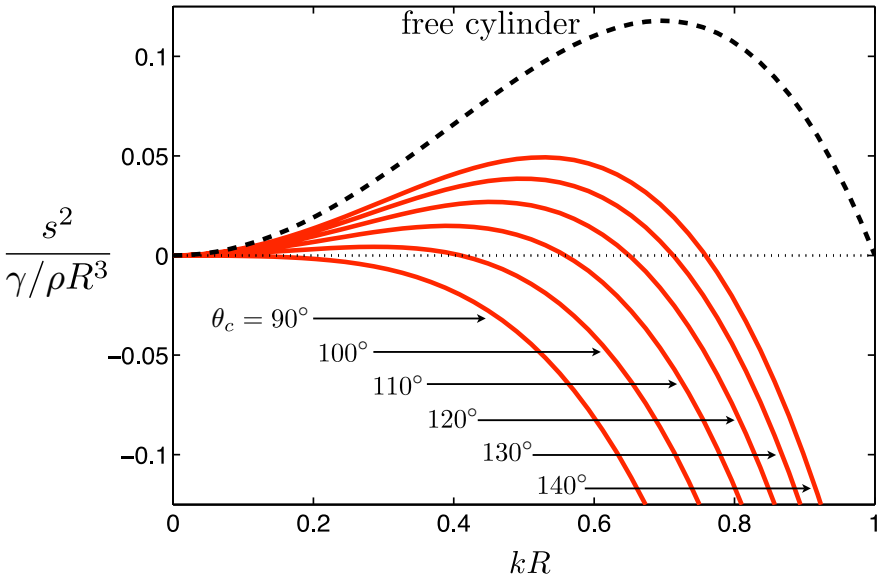

Figure 8. Capillary instability of cylindrical segment on a wedge: square of the dimensionless growth rate of the most unstable mode, $s^2/(\gamma/\rho R^3)$, as a function of the dimensionless wavenumber, kR, for various value of the apparent angle of the stripe, $\theta_c = 90°$, 100°, 110°, 120°, 130° and 140°. We also reproduce in dashed line the growth rate for a free cylinder (classical Rayleigh–Plateau instability).

At the contact points, $\{r = R, \theta = 0, 2\theta_c\}$, equation (22) becomes

$$\sum_{n=0}^{\infty} A_n I'_{\lambda_n}(kR) = 0. \tag{40}$$

As above, we obtain a generalized eigenvalue problem for the eigenvalue s^2 and the eigenvector A_n. We can combine equations (39) and (40) by writing them as

$$\sum_{n=0}^{\infty} A_n a_n(\theta) = s^2 \sum_{n=0}^{\infty} A_n \alpha_n(\theta), \tag{41}$$

where the coefficients a_n and α_n are defined as

$$a_n(\theta) = \begin{cases} \frac{\gamma}{\rho R^2} k \left(1 - k^2R^2 - \frac{n^2\pi^2}{4\theta_c^2}\right) I'_{\lambda_n}(kR) \cos\frac{n\pi\theta}{2\theta_c}, & 0 < \theta < 2\theta_c, \\ I'_{\lambda_n}(kR), & \theta = 0 \text{ or } \theta = 2\theta_c, \end{cases} \tag{42}$$

$$\alpha_n(\theta) = \begin{cases} I_{\lambda_n}(kR) \cos\frac{n\pi\theta}{2\theta_c}, & 0 < \theta < 2\theta_c, \\ 0, & \theta = 0 \text{ or } \theta = 2\theta_c. \end{cases} \tag{43}$$

As above, an approximate solution can be found by truncating the series at $n = N$ and evaluating equation (41) at $N+1$ values of θ, which include $\theta = 0$. In the matrix form, the truncated

eigenvalue problem is now given by

$$\begin{bmatrix} a_0(\theta_1) & \cdots & a_N(\theta_1) \\ \vdots & & \vdots \\ a_0(\theta_{N+1}) & \cdots & a_N(\theta_{N+1}) \end{bmatrix} \begin{bmatrix} A_0 \\ \vdots \\ A_N \end{bmatrix} = s^2 \begin{bmatrix} \alpha_0(\theta_1) & \cdots & \alpha_N(\theta_1) \\ \vdots & & \vdots \\ \alpha_0(\theta_{N+1}) & \cdots & \alpha_N(\theta_{N+1}) \end{bmatrix} \begin{bmatrix} A_0 \\ \vdots \\ A_N \end{bmatrix}. \tag{44}$$

By numerically solving this eigenvalue system, we find that such a cylindrical wedge of fluid is stable as long as the opening of the wedge satisfies $\theta_c < 90^\circ$. When $\theta_c \geqslant 90^\circ$ we find unstable modes, and the square of their dimensionless growth rates are displayed in figure 8 as a function of the dimensionless wavenumber of the perturbation (solid lines). As above, we have included the classical Rayleigh–Plateau result (dashed line). We see that the growth rate of the most unstable modes in this set-up (wedge-like stripe) is very similar to the ones obtained in the previous section (horizontal stripe). In particular, we recover the result that in the limit where the angle $\theta_c \to 90^\circ$, the most unstable perturbation wavelength increases to infinity. Note that the stability transition obtained in this configuration is not a transition in the apparent contact angle, but instead a transition in cross-sectional shape of the fluid segment.

5. Conclusion

In this paper, we have studied the dynamics of the capillary instability discovered experimentally by Gau *et al* [5]. In that work, it was shown that a circular segment of fluid located on a hydrophilic stripe on an otherwise hydrophobic substrate becomes unstable when its volume reaches that at which its apparent contact angle on the surface is 90°. Instead of breaking up into droplets, the instability leads to the excess fluid collecting into a single bulge along each stripe. By performing a linear stability analysis of the capillary flow problem in the inviscid limit, we have first reproduced previous results showing that the cylindrical segment is linearly unstable if (and only if) their apparent contact angle is larger than 90°. We have then calculated the growth rate of the instability as a function of the wavenumber of the perturbation, and shown that the most unstable wavenumber for the instability—the one which would therefore be observed in an experimental setting—decreases to zero when the apparent fluid contact angle reaches 90°, allowing us to re-interpret the creation of bulges in the experiment as a zero-wavenumber capillary instability [5, 18]. A variation of the stability calculation was also considered in the case of a hydrophilic stripe located on a wedge-like geometry. Since droplets of any shape can now be created experimentally using chemical substrate modification [19], the stability of more complex fluid topologies could be analyzed using a framework similar to the one developed here.

Acknowledgments

We thank Professor Lipowsky for allowing us to reproduce in figure 1 the picture from [5]. This work was funded in part by the National Science Foundation (grants CTS-0624830 and CBET-0746285 to Eric Lauga).

References

[1] Eggers J 1997 Nonlinear dynamics and breakup of free-surface flows *Rev. Mod. Phys.* **69** 865–929

[2] Drazin P G 2002 *Introduction to Hydrodynamic Instability* (Cambridge: Cambridge University Press)

[3] de Gennes P-G, Brochard-Wyart F and Quéré D 2004 *Capillarity and Wetting Phenomena: Drops, Bubbles, Pearls, Waves* (New York: Springer)

[4] Pomeau Y and Villermaux E 2006 Two hundred years of capillarity research *Phys. Today* **59** 39–44

[5] Gau H, Herminghaus S, Lenz P and Lipowsky R 1999 Liquid morphologies on structured surfaces: from microchannels to microchips *Science* **283** 46–9

[6] Davis S H 1980 Moving contact lines and rivulet instabilities. I. The static rivulet *J. Fluid Mech.* **98** 225–42

[7] Brown R A and Scriven L E 1980 On the multiple equilibrium shapes and stability of an interface pinned on a slot *J. Colloid Interface Sci.* **78** 528–42

[8] Roy R V and Schwartz L W 1999 On the stability of liquid ridges *J. Fluid Mech.* **391** 293–318

[9] Lenz P 1999 Wetting phenomena on structured surfaces *Adv. Matter.* **11** 1531–4

[10] Lipowsky R, Lenz P and Swain P S 2000 Wetting and dewetting of structured and imprinted surfaces *Colloids Surf.* A **161** 3–22

[11] Lenz P and Lipowsky R 2000 Stability of droplets and channels on homogeneous and structured surfaces *Eur. Phys. J.* E **1** 249–62

[12] Brinkmann M, Kierfeld J and Lipowsky R 2004 A general stability criterion for droplets on structured substrates *J. Phys. A: Math. Gen.* **37** 11547–73

[13] Darhuber A A, Trojan S M, Miller S M and Wagner S 2000 Morphology of liquid microstructures on chemically patterned surfaces *J. Appl. Phys.* **87** 7768–75

[14] Schiaffino S and Sonin A A 1997 Formation and stability of liquid and molten beads on a solid surface *J. Fluid Mech.* **343** 95–110

[15] Langbein D 1990 The shape and stability of liquid menisci at solid edges *J. Fluid Mech.* **213** 251–65

[16] Brinkmann M and Blossey R 2004 Blobs, channels and 'cigars': morphologies of liquids at a step *Eur. Phys. J.* E **14** 79–89

[17] Yang L and Homsy G M 2007 Capillary instabilities of liquid films inside a wedge *Phys. Fluids* **19** 044101

[18] Koplik J, Lo T S, Rauscher M and Dietrich S 2006 Pearling instability of nanoscale fluid flow confined to a chemical channel *Phys. Fluids* **18** 032104

[19] Jokinen V, Sainiemi L and Franssila S 2008 Complex droplets on chemically modified silicon nanograss *Adv. Mater.* **20** 3453–6